ADVANCED FUNCTIONAL MATERIALS

Supporting Information

Eliminating Local Electrolyte Failure Induced by Asynchronous Reaction for High-Loading and Long-Lifespan All-Solid-State Batteries

Hanwen An, Qingsong Liu, Biao Deng, Jian Wang, Menglu Li, Xin Li*, Shuaifeng Lou* and Jiajun Wang*

Eliminating Local Electrolyte Failure induced by Asynchronous Reaction for High-Loading and Long-Lifespan All-Solid-State Batteries

Hanwen An, Qingsong Liu, Biao Deng, Jian Wang, Menglu Li, Xin Li*, Shuaifeng Lou*, Jiajun Wang*

H. W. An, Q. S. Liu, M. L. Li, S. F. Lou, J. J. Wang

MIIT Key Laboratory of Critical Materials Technology for New Energy Conversion and Storage, School of Chemistry and Chemical Engineering, Harbin Institute of Technology, 150001 Harbin, China.

E-mail: shuaifeng.lou@hit.edu.cn   jiajunhit@hit.edu.cn

X. Li

John A Paulson Sch Engn & Appl Sci, Cambridge, Harvard University, MA 02138 USA.

E-mail: lixin@seas.harvard.edu

H. W. An, Q. S. Liu, S. F. Lou, J. J. Wang

Chongqing Research Institute of HIT, Chongqing 401135, P. R. China.

B. Deng

Shanghai Institute of Applied Physics, Chinese Academy of Sciences, 239 Zhangheng Road, Shanghai, 201204, China.

J. Wang

Canadian Light Source Inc., University of Saskatchewan, Saskatoon, SK S7N 2V3, Canada.

Abstract

The design of practical cathodes with high areal capacity in polymer-based all-solid-state batteries remains challenged by the absence of an effective guiding principle that prolongs battery life-span. Unlike liquid batteries, the notorious interface incompatibility between

1

cathodes and electrolytes limited the cycling life of the all-solid-state batteries. Herein, we proposed a dynamically stable cathode design with a fully covered surface, effectively mitigating interface failure and enabling the cyclic time of batteries with a cathode loading of 12.7 mg cm^{-2} over 10,000 hours. Our work unveils the importance of local state of charge in affecting the interfacial properties of particles through local oxidative-stability of electrolytes on the interface. We show that the phenomena can be strongly influenced by the porosity of the cathode through the perspective of discreteness of ion transport. Our insights and approach provide a broader promise for solid batteries for long lifetime.

1. Introduction

The urgent demand for high security and high energy density has put unparalleled emphasis on the rapidly developing all-solid-state lithium batteries (ASSLB)[1]. Solid polymer-based batteries are advantageous as low-cost and industrially producible alternatives for future energy storage[2]. As a critical component of the ASSLB, the solid-state composite cathode[3] directly determines the output capacity and energy density. Increasing the loading of the state-of-the-art layered LiNi$_{0.8}$Co$_{0.1}$Mn$_{0.1}$O$_2$(NCM) materials[4] can increase the energy density for practical applications. Unfortunately, there is a notorious adaptability challenge between NCM and conductive polymer electrolyte[5]. Especially in thick composite cathodes, dramatically fast capacity fading[6] rendered NCM unsuitable for polymer batteries.

The conventional studies of capacity fading for the cathodes has focused on the chemical failure due to the inherent instability of electrolyte[7]. Recently, our group found that the state of charge (SOC) inhomogeneity within active particles and loss of structural integrity evoked by local physical contact[8] can eventually lead to the deactivation of sub-particle level domains, while some other study elaborated on the evolution of physical cracks of particle structure induced by the inhomogeneity of its SOC during charging[9]. Nevertheless, the correlation between chemical evolution at the NCM-electrolyte interface and electrode physical structure was disregarded. As a key parameter of solid-state cathode, the contact area between NCM and conductive binder domain (CBD), plays crucial roles on the interface stability of composite cathodes[3b], yet the structure-activity relationship between contact area and interface stability is still poorly understood. In previous study of high loading cathodes, local micro-architecture was rarely considered. We speculate that it is strongly correlated to ion transport discreteness and capacity fading. Thus, for manufacturing high performance electrodes, a deep understanding of the local structure and charge state of cathode and its interplay with interface evolution is imperatively required.

Here we diagnosed that the oxidative decomposition behavior of electrolytes is correlated with local structure and state of electrode particle. Cathodes with differential contact interface were investigated to demonstrate the inconceivable distinction of chemical evolution at the local contact interface. Porous electrodes with isolated contact surfaces with electrolytes display discrete ion transport, which results that the Ni^{4+}-rich region is exposed at the point contact surface of NCM particle with electrolyte. Then the electrolyte was preferentially decomposed into non-conductive interface, a fast capacity fading occurred. In contrast, electrodes with homogeneous contact exhibit homogeneous particle-scale SOC and higher oxidation stability. Hence, a stable interface can be achieved by simultaneously increasing surface coverage by electrolyte and improving the inherent stability of electrolyte. Accordingly, a high-loading composite cathode (12. mg cm^{-2} and 28.6 mg cm^{-2}) with fully active surface was designed via a solvent-free in-situ liquid-solid transformation strategy. Benefiting from the dual modification of physical structure remodeling and chemical methods, the design enables high-loading $LiNi_{0.8}Co_{0.1}Mn_{0.1}O_2$ cells to exhibit an excellent lifespan over 10,000 hours (500 cycles with retention of 70%). The battery with a cathode loading of 28.6 mg cm^{-2} cycled up to 150 times.

2. Results and Discussion

Blocked local ion transport in cathode after cycling

In solid-polymer cathode (SPC) manufacturing process, the calendaring is also introduced in SPC to increase the contact area between conductive-binder domain (CBD, polymer electrolyte and carbon) and cathode particles for low interface impedance. For ASSLB using polyethylene oxide (PEO) as the electrolyte, hot-calendaring is generally employed to reduce porosity[10]. In this study, polycrystalline $LiNi_{0.8}Co_{0.1}Mn_{0.1}O_2$ (NCM) particles with an average size of 10-20 μm were selected as active materials (**Figure S1**). Hence, high-loading composite cathodes with different active surface were prepared by calendaring and hot-calendaring processes, respectively, to explore the evolution discrepancy of interfacial behavior. As shown in **Figure 1a** and **b**, NCM particles in the calendaring cathode (Cal) were partially covered by CBD, while those in the hot-calendaring cathode (Hot-Cal) were almost fully covered.

The batteries assembled by Cal and Hot-Cal exhibit differences in charge/discharge capacity in **Figure 1c**. We find that they also show discrepant ion transport rates (**Figure S2**) from impedance measurement. This suggests Cal and Hot-Cal may induce different levels of contact inhomogeneity, as illustrated in **Figure 1d** and **e**. Correspondingly, the Cal battery displays a transitory voltage plateau at 3.8 V (**Figure 1c**) likely caused by certain decomposition reactions

during the first charge (constant current), which differs from the liquid batteries and Hot-Cal batteries. Previous studies proposed that this phenomenon was highly related to the oxidative instability of PEO-based electrolytes[7]. However, the disappearance of such a plateau in the charging curve of Hot-Cal batteries with the same composition seems to suggest that PEO is stable at 3.8 V while the issue is at the cathode-electrolyte interface in Cal batteries.

The galvanostatic intermittent titration technique (GITT) was conducted during the initial two charge/discharge[11]. A series of ion diffusivity (D_1) versus voltage in **Figure 1f** was obtained from GITT data (**Figure S3**), in which the D_1 is a normalized diffusion coefficient to describe the ion diffusion rate at the interface (See Methods). Compared to Hot-Cal, a slightly sluggish ion diffusion of Cal may be ascribed to heterogeneous interfacial contact. Nonetheless, the subsequent cycling reaction kinetics of the Cal cathode is more hindered after the first cycle, featured by an obvious drop in ion diffusivity during the second cycle. This phenomenon further supports the schematic depicted in **Figure 1d** and **e**, where the CBD on the local contact surface in the Cal cell may be converted to non-conductive phase after the first charging. Furthermore, Hot-Cal cells displayed a lifetime of 50 cycles with a capacity retention of 67.5%, while the Cal cells exhibit significant performance degradation with no capacity after 32 cycles (**Figure 1g**). The large difference may be closely related to the abnormal voltage plateau at 3.8 V during initial charge/discharge. Overall, the results indicate that the cycling stability of composite cathodes is distinctly dominated by the initial charge/discharge process and local microstructures.
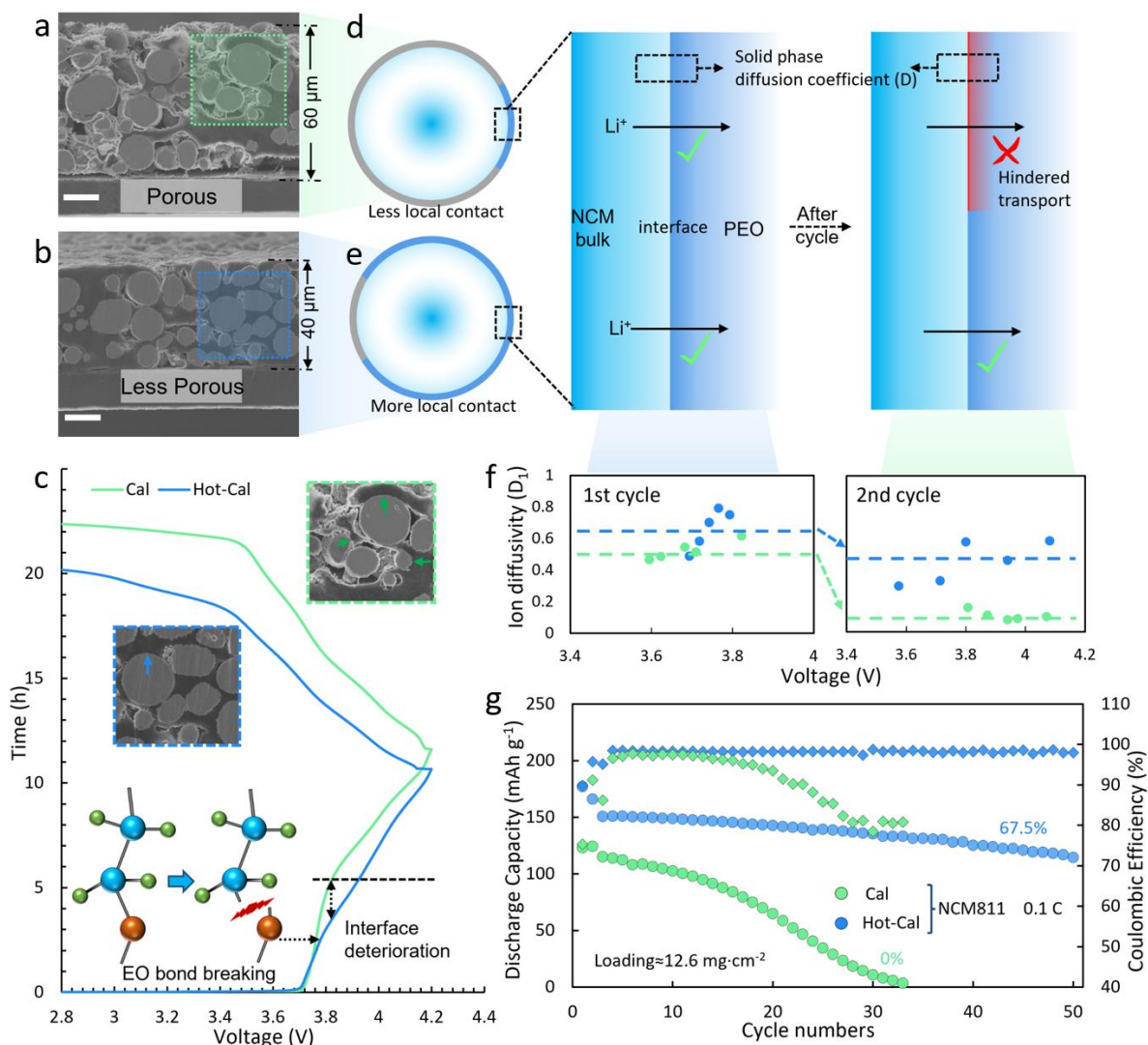
Figure 1. Blocked ion transport in calendaring cathode after cycling. (a) Scanning Electron Microscope image of calendaring cathode and (b) Hot-calendaring cathode, scale bar 15 µm. (c) First charge-discharge curve of the composite cathodes. (d) Schematic of ion transport behavior in calendaring cathode and (e) Hot-calendaring cathode. (f) Comparison of Li-ion diffusion coefficient after the first cycle. (g) Cycle performance.

Quantitative analysis and interfacial local electrochemical failure

To obtain more direct information on the correlative behavior between cathode architecture and electro-properties, a quantitative analysis of active surface and interface characteristics is conducted by synchrotron X-ray imaging technology. By adjusting the grey level between NCM and CBD (X-ray absorption of substances is NCM, CBD, Pores), the structure of the interface was reconstructed (shown in **Figure 2a**). As shown in **Figure 2b**, the virtual slice of the individual components (NCM, CBD and pore) is distinguishable due to their different attenuation to X-rays. Here the direct contact interface between NCM particles and CBD is

defined as the active surface (or active area), and the exposed interface to pores with no contact is defined as the inactive surface **(Figure 2c)**. Three-dimensional reconstruction imaging displays identical real volume and surface area of the two NCM cathode from Cal cathode and Hot-Cal cathodes (**Figure 2d**), whereas the Cal cathode show a smaller area of the active surface compared to Hot-Cal cathode (**Figure 2e).** Considering the the same components and similar charge/discharge performance and oxidative stability of these two electrodes, as summarized in **Figure 2f,** and close NMC and CBD volume (**Figure 2g**), the obvious increase of battery performance after Hot-Cal is speculated to be caused by the smaller pore volume and the related larger active area, (**Figure 2g and h**), suggesting that these factors can strongly influence interface reactions of inactive or active areas.
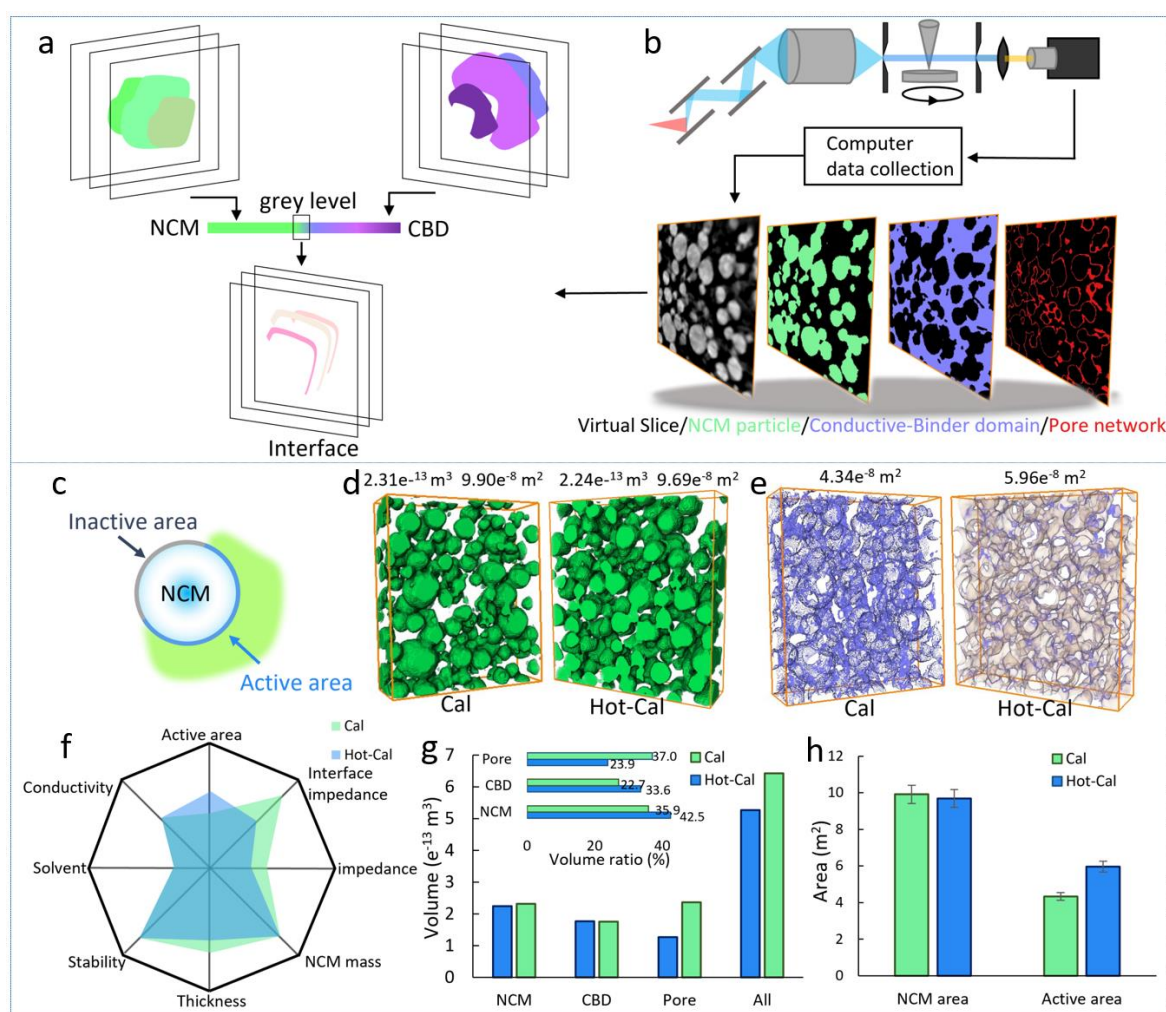
Figure 2. Quantitative analysis of the active area of Cal cathodes and Hot-Cal cathodes. (a) The principle of reconstructing interface from grey level. (b) Synchrotron X-ray tomography virtual slice and corresponding phase of the cathode. (c) Schematic of inactive/active surface. (d) 3D microstructure of NCM and (e) active area shown by tomography reconstruction with volume rendering, the viewport size of all presentation structures is $200{\times}200$ µm^2. (f)

Comparison of physicochemical parameters of cathodes (Solvent: Residual acetonitrile solvent in electrolyte, Thickness: Electrode thickness; Conductivity: Ionic conductivity of CBD). (g) The volume ratio of each phase based on synchrotron x-ray tomography. (h) The proportion of active area on the NCM surface.

To further investigate charge transfer reactions at cathode interfaces, in-situ Fourier transform infrared spectroscopy (FTIR, absorption mode) was performed to track the idiographic chemical variation (the in-situ FTIR cell structure is shown in **Figure S4**). As the Potential-Wavenumber graphics of Cal batteries in **Figure 3a**, the absorption peaks at 1200 cm^{-1}, 1275 cm^{-1} and 1320 cm^{-1} appear when the charging voltage reaches about 3.8 V, which correspond to the oxidation impurities of PEO-based electrolyte, CF$_3$-R, CF$_3$-SO$_2$-O-CH$_2$-R and SO$_2$-R[12]. Contrary to Cal batteries, no obvious oxidative decomposition product in the Hot-Cal batteries was observed (**Figure 3b, c and d**).

The continuous deterioration of PEO can trigger the formation of non-conductive interface on the active area in Cal batteries (Figure 3e), and an incremental interfacial resistance with battery charging. Hence, we conducted in-situ electrochemical impedance spectroscopy (EIS) test to evaluate the ion transport kinetics at different charging voltages. As the EIS presented in Figure 3f, the two electrodes exhibit similar values of membrane impedances before charging, and the slight difference could be ascribed to the variant thickness of the electrolyte membrane. In the mid-frequency range of EIS in ASSLB, the diameter of the semicircular arc is considered to be the interface impedance[13]. Owing to the more discontinuous contact, Cal batteries exhibits a higher initial interfacial impedance compared to Hot-Cal. With charging, the Cal batteries showed a continuous interfacial impedance growth, which is consistent with the decomposition of electrolyte as detected by our FTIR. On the contrary, no significant increase of impedance in Hot-Cal electrode was observed. Previous research suggested that the cycling degradation is related to the oxidation instability of PEO, while our results here demonstrate that a proper design of cathode microstructure by Hot-Cal can mitigate the degradation, which seems to question the assumption that such decomposition is caused by the voltage instability of PEO.

To gain more explicit insights into the degradation mechanisms of the Cal batteries, we employed a confocal Raman system to characterize the particle-scale SOC. The phase transition of the active material NCM could be estimated by the intensity ratio of Eg/ A1g in Raman spectroscopy, where higher Eg/ A1g ratio can indicate more higher SOC of the NCM particle[14]. For the Cal cathode before cycle, both good and poor contact particle (**Figure S5**) feature very close ratio of E$_g$/A$_{1g}$, as the Raman spectroscopy shown in **Figure 3g and h**. The poor-contact

particles demonstrate an increase of E_g/A_{1g} while the good-contact particles have the same ratio after 20 cycles (**Figure 3h**). The phenomena suggests that poor-contact particles in Cal are more prone to increased SOC after cycling, most probably caused by blocked Li^+ intercalation in discharge. Combined with the results of electrolyte deterioration confirmed by FTIR for the cathode region in the Cal cell, we deduce that the electrolyte is decomposed at the active area of poor-contact particles due to the higher local SOC.
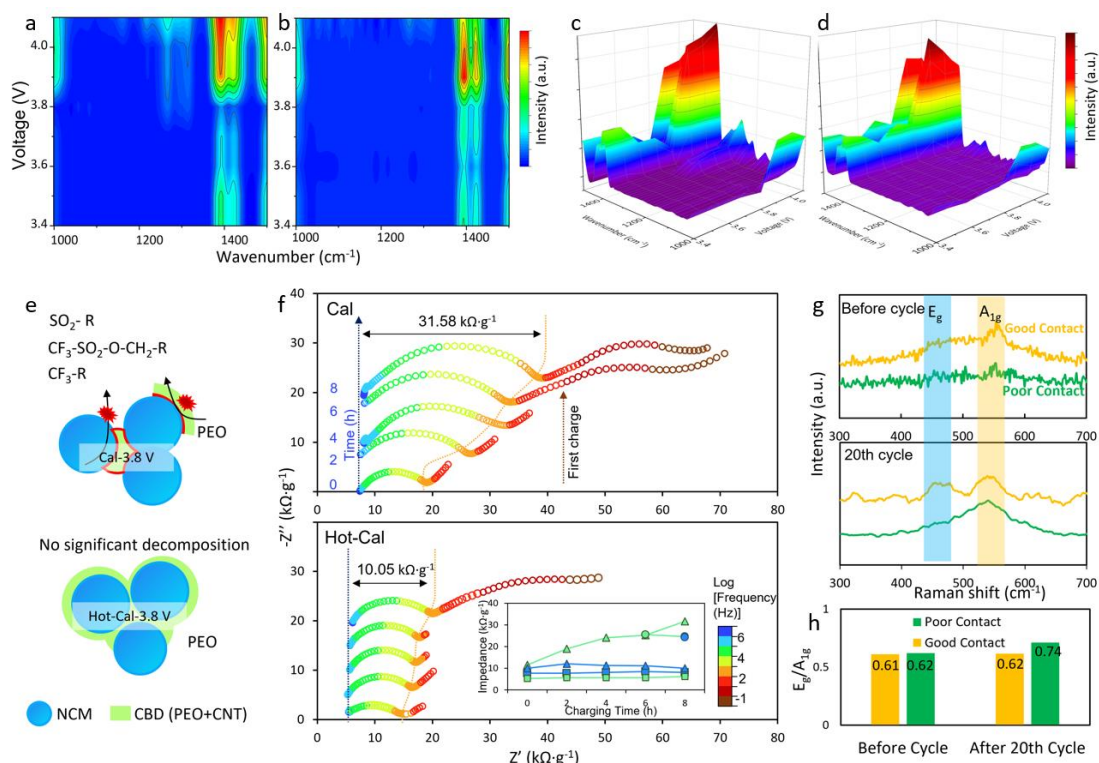
Figure 3. Interfacial chemical failure of the Cal cathodes with local ion transport. (a) In-situ FITR spectrum of calendaring cathode and (b) Hot-calendaring cathode. (c) 3D FITR of calendaring cathode and (d) Hot-calendaring cathode. (e) Schematic of local chemical failure on NCM particle during charging. (f) Comparison of interface impedance evolution during first charging, as well as the image of poor contact and good contact particle. (g) Raman spectrum of particles before and after cycling. (h) Comparison of intensity ration of E_g/A_{1g}.

Electrolyte failure induced by local region of high delithiation state

Delithiation reactions (Ni^{3+} to Ni^{4+}) in solid-state batteries rely on Li^+ transport through the active surface during charging, the NCM particle of Cal batteries with both inactive and active areas (Figure 4a and c) reacts preferentially on the active surface due to the isolated ion transport[6a]. Consequently, a Li^+ concentration gradient at the particle scale was formed at the same electrode potential (or degree of delithiation), indicating a higher Ni^{4+} concentration at the active surface (Figure 4e). In contrast, NCM is more evenly wrapped (Figure 4b and d) in

8

Hot-Cal cells, inducing a more homogeneous distribution of Ni^{4+} at the particle level (Figure 4f), and thus less local Ni^{4+} concentration at a given SOC. This can cause drastic differences in the electrochemical stability at local interfaces. For example, transition metal (TM) elements with high valence may play a role in accelerating the catalytic decomposition of organic electrolytes (Figure 4g) [7a, 15]. Using interface stability calculation based on the standard pseudo-binary approach[16], the interface reaction between electrolyte and NCM is calculated (**Figure S6**) with the interface reaction energy presented in **Figure 4h**. With the increase in the degree of delithiation, the energy gradually decreases, indicating a higher reactivity between the PEO-based electrolyte and Ni^{4+} on the NCM surface.

Moreover, confocal Raman spectroscopy was carried out again to further investigate electrolyte degradation inside Cal electrodes, in light of the comparative analysis shown in **Figure 4i and j**. The band at 734 cm^{-1}, a response of interaction between $TFSI^-$ and TM, shifted and disappeared after cycling for poor-contact particles[17]. This demonstrate that the interaction between LiTFSI and NCM disappears, and LiTFSI decomposes, resulting in a series of deterioration effects of the electrolyte. However, the signal of interaction for good-contact particles are still visible after cycling. By comparing the above results, the discrepant Ni^{4+}/Ni^{3+} ratios caused by the inhomogeneity of Li^+ transport may be the key factor leading to the interface failure.

To further validate the formation of the local region with a high ratio of Ni^{4+}/Ni^{3+}, synchrotron scanning transmission X-ray microscopy (STXM) was employed to reveal the local distribution of Ni element in the two cathodes (Cal and Hot Cal). The STXM can provide high-resolution soft X-ray absorption spectroscopy (XAS) of two-dimensional spatial distribution[18]. As shown in **Figures 4k-n**, the ptychography of the Cal cathode (**Figure 4k**) reveals that region 1 and 2 exhibits a higher X-ray absorption degree than that in the regions 3 and 4 due to the high concentration of Ni^{4+}. Moreover, **Figure 4m** draws the Ni^{4+} rich areas (red) corresponding to region 1 and 2, and rich Ni^{3+} areas (green) corresponding to region 3 and 4. By contrast, the ptychography of the Hot-Cal cathode (**Figure 4l and n**) displays a uniform phase distribution, which can be confirmed by the corresponding XAS spectra of Ni L-edge at different regions (**Figure 4o and p**). For the particle of Cal cathode, region 1 shows a high-intensity ratio of Ni^{4+}/Ni^{3+} (1.37), but region 4 shows a low ratio of 0.75. In contrast, the particle of Hot-Cal illustrates a relatively average ratio of Ni^{4+}/Ni^{3+} (0.97~1.07). The intensity ratio of Ni^{4+}/Ni^{3+} of the particle in Cal is downgraded along the direction of regions 1 to 4, and the ratio of region-1 in Cal batteries is higher than the ratio of any region of the particle in Hot-Cal (**Figure 4q**).

By combining the theoretical calculation, we conclude that the local contact leads to a Ni^{4+}-rich region at the interface during charging for the cathode with the heterogeneous inner physical contact of ASSLB. Therefore, the SOC of local contact region is higher than the apparent SOC of the overall electrode, which is asynchronous charge equilibration effects. The generation of a high concentration of Ni^{4+} promotes interfacial reactivity and exacerbates the decomposition of organic electrolytes. This also explains that the actual working potential of PEO is much lower than the electrochemical oxidation stability window under Linear Sweep Voltammetry (LSV) test (**Figure 4r**).
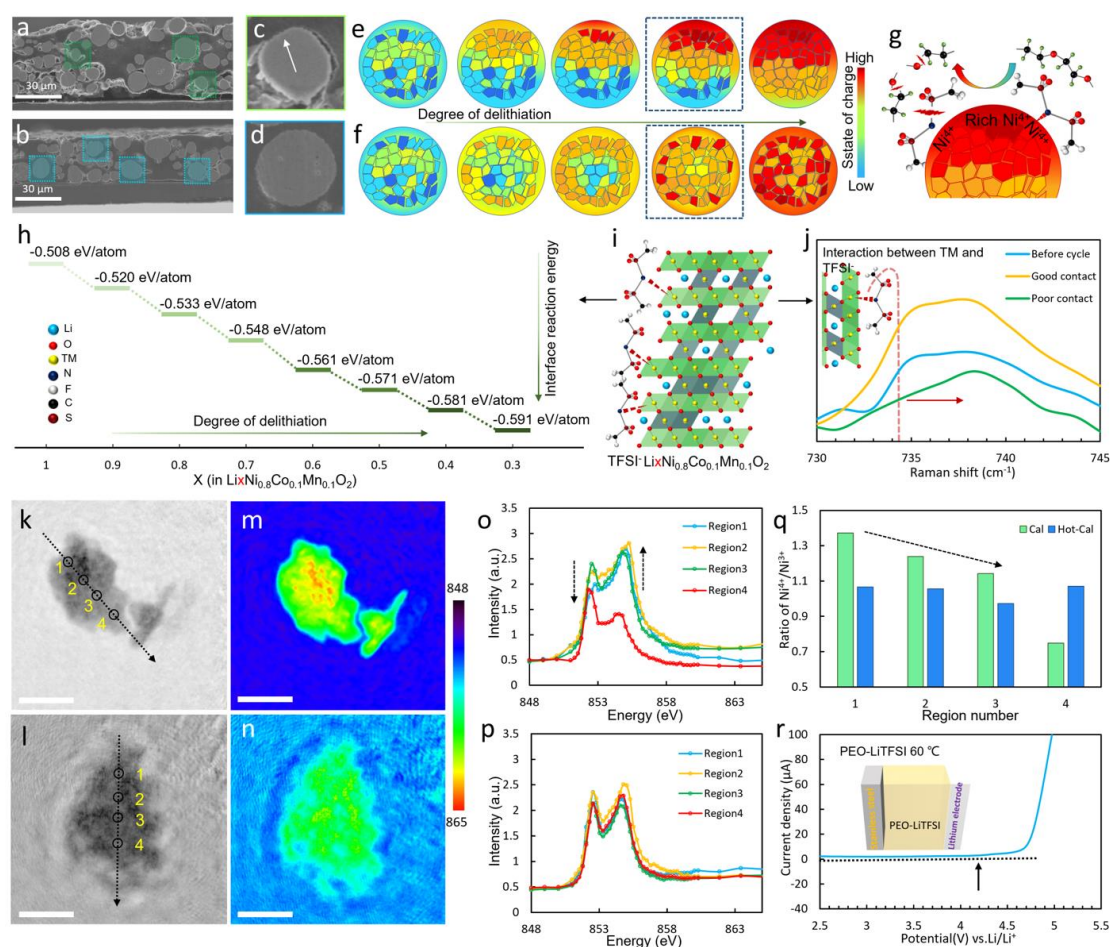
Figure 4. High state of charge in particle scale at local contact accelerates the decomposition of electrolyte. (a) Scanning Electron Microscope image of calendaring cathode and (b) Hot-calendaring cathode, scale bar 30 µm, and the (c) local contact NCM particle, (d) evenly wrapped particle. (e) Schematic of SOC distribution during charging corresponding to local contact NCM particle and (f) evenly wrapped particle. (g)The decomposition of electrolyte on the surface with a high concentration of Ni^{4+}. (h) Interface reaction energy between $Li_xNi_{0.8}Co_{0.1}Mn_{0.1}O_2$ and $TFSI^-$. (i) Adsorption of $TFSI^-$ and transition metal elements. (j) Raman spectrum of particles before and after cycling. (k) Ptychography STXM amplitude

(optical density) image of the particle in calendaring batteries and (l) Hot-calendaring cathode, disassembled from the full cell at the stable voltage of 4 V, the viewport size is 2.5×2.5 μm². (m) Elemental distribution mapping at the Ni edges of NCM particle in Cal batteries and (n) Hot-Cal batteries. (o) XAS spectra of Ni L3-edge in different regions extracted from Figure 4m and (p) from Figure 4n. (q) Quantification of the Ni^{4+}/Ni^{3+} intensity ratio along region-1 to region-4. (r) Linear sweep voltammetry of PEO-LiTFSI.

Dynamically stable design for long life batteries

To avoid unfavorable inactive surface during solvent evaporation **(Figure S7a)**, the solvent-free method seems to be more suitable for the preparation of polymer-based solid-state composite electrodes[19]. Besides, adopting an interfacial modification strategy is necessary to improve the compatibility considering the intrinsic chemical stability of PEO and NCM. Both the active area and intrinsic electrochemical stability need to be considered for solid-state battery matching high-voltage positive electrode, and this strategy also has certain guiding significance for inorganic solid-state battery.

Herein, the cathode with a fully active surface is designed by an in-situ liquid-solid transformation approach to prevent asynchronous charge equilibration. Specifically, in the cathode slurry compounding process, a solvent-free and liquid ion-conductive mixture, containing PEO derivatives (poly(ethylene glycol)diacrylate, PEGDA) , nitrile-based additives (ethyl cyanoacrylate, ECA) and Li salt, was used as dispersants to obtain uniform cathode slurries (**Figure S7b, Figure S8**). The liquid is then transformed into a conductive polymer in homogeneous and intimate contact with the NCM via in-situ thermal polymerization. Meanwhile, nitrile-based additive as interpolymer is used to stabilize the NCM-electrolyte interface. This "two-pronged" approach enables homogeneous interfacial ion transport and high-voltage interfacial stability inside the polymer-based solid-state composite cathode.

FTIR was conducted to confirm the interaction between NCM and poly(ethyl cyanoacrylate) (PECA). In **Figure S9**, the disappeared peak of the $-C \equiv N$ group at 2252 cm^{-1} indicates the adsorption of PECA on NCM. The adsorption sites of the Ni atom are occupied by the $-C \equiv N$ group that replaces the TFSI$^-$, which stabilize the interface due to the remission of TFSI$^-$ decomposition[20]. The high stability of ECA on the surface of NCM is verified by the calculated interfacial reaction energies (**Figure S10**). Furthermore, the long cycle life can benefit from the high electrochemical window (>5.3 V, **Figure S11a**) and fast conductivity (0.43 mS cm^{-1}, **Figure S11b-c**) of the copolymer poly(ethylene glycol)diacrylate-poly(ethyl cyanoacrylate)

(PEGDA-PECA), and the battery showed excellent discharge capacity at 30-100°C (**Figure S11d**). Besides, a copolymer containing a mass fraction of 5% ECA is selected as the CBD base because of its good electrical conductivity and oxidation resistance (**Figure S11e**)..

Importantly, the NCM particles in the composite cathode PEGDA-PECA-NCM (PCA) are homogeneously wrapped and intimately contacted with the conductive-binder domain (**Figure S12**). The synchrotron X-ray imaging (**Figure 5a and b**) shows an extremely lower pore volume of PCA cathode (0.30×10^{-14} m^3), in contrast to both Cal cathode (3.65×10^{-14} m^3) and Hot-Cal cathode (2.21×10^{-14} m^3), which means an even SOC of each particle during charging can be expected. Although the decomposition of electrolytes at the interface is inevitable, dynamic stability can be achieved by tailoring fully active surface cathode.

Consequently, an impressive long cyclic life over 500 cycles with an ultra-high loading of 12.7 mg cm^{-2} (0.1 C) is demonstrated in the full cell assembled by LiNi$_{0.8}$Co$_{0.1}$Mn$_{0.1}$O$_2$ as active materials, PEO-Li$_{6.4}$La$_3$Zr$_{1.4}$Ta$_{0.6}$O$_{12}$ as electrolyte membrane (**Figure 5c, d and Figure S12c, d**). It is noteworthy that the charge and discharge curves were flat and the voltage polarization remained small after long cycles (**Figure S12e, f and Figure S13a**). This ultra-long cyclic time (over 10,000 hours, **Figure 5e, Figure S13b**) provides strong evidence for the oxidation resistance of PCA cathodes. In addition, higher loading (28.6 mg cm^{-2}) of PCA batteries exhibited discharge specific capacity of more than 160 mAh g^{-1} (4.85 mAh cm^{-2}) at 0.2C, cycled up to 150 cycles (retention of 77.9%, **Figure S14a**). The cyclic performance of the dual-modified cathode is better than that of the single-modified cathode (PEGDA cathode: homogeneous contact but insufficient oxidation stability; and PEO-CAN: high oxidation resistance but insufficient active area, **Figure S14b**). **Figure S15** showed the unprecedented performance of this work relative to the reported PEO high voltage batteries[7a, 7b, 12, 21]. These results suggest that devising the electrode with the fully active surface is a promising route enabling high-energy-density ASSLB in practical industrial applications.
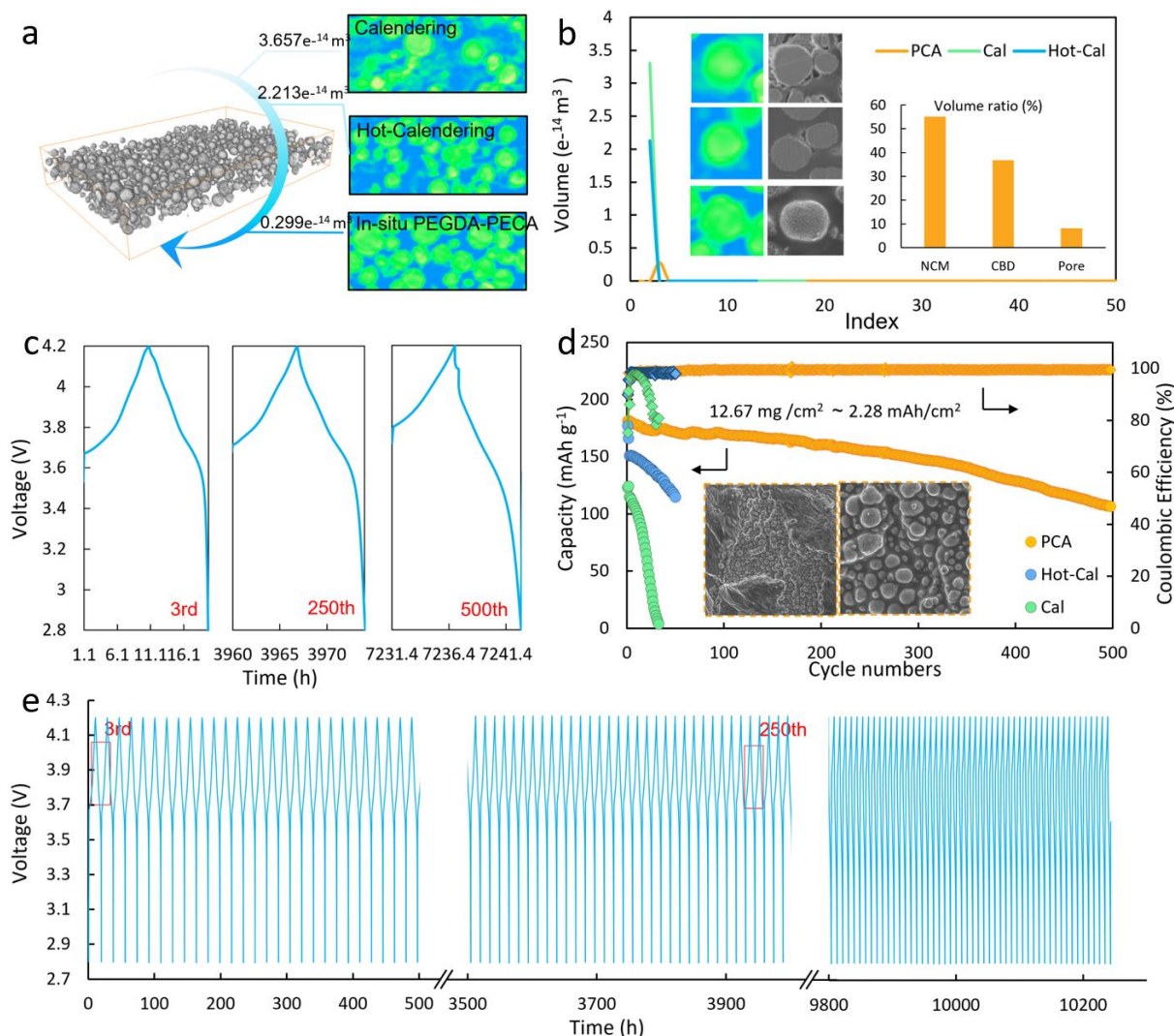
Figure 5. Fully active surface design for stable interface and battery performance. (a) 3D reconstruction of PCA and slice of Cal, Hot-Cal, and PCA. (b) Index-volume curve extracted from the 3D reconstruction of different cathodes. (c)The 3rd, 250th, 500th time-voltage curve of PCA. (d) Cyclic performance of ASSLBs with Cal, Hot-Cal, and PCA cathode, and the surface morphology of PCA, scale bar, 100 µm, 30 µm. (e) Time-voltage curve of PCA.

3. Conclusion

In summary, we revealed the unique correlation between local microstructure and interfacial chemical stability in solid-state cathodes. Overall results demonstrate that the actual electrochemical oxidation-reistance stability of the electrolyte is severely affected by the local structure and charge state inside the solid-state electrode. The localized transport results in severe inhomogeneity of particle-scale SOC and asynchronous charge equilibration. Thereby a continuous degradation of the conductive-binder domain is exacerbated by high-valence transition metals on the local surface of active materials, leading to irreversible capacity loss

13

and reduced cycle life. After manipulating the area of the active surface and improving the electrochemical window of the electrolyte to achieve a kinetically stable interface, excellent charge-discharge time over 10,000 h of the composite cathode with 12.7 mg cm^{-2} loading was obtained, and the cathode with higher areal capacity (28.6 mg cm^{-2}, 4.85 mAh cm^{-2}) also exhibits a cycle life over 150 cycles. Our study provided both insights into the degradation mechanism of electrolytes and a promising route to develop high-energy-density ASSLB.

4. Experimental Methods

All experimental details are included in the Supporting Information.

Supporting Information

Supporting Information is available from the Wiley Online Library or from the author.

References

[1] a)L. Ye, X. Li, *Nature* **2021**, 593, 218; b)S. Randau, D. A. Weber, O. Kötz, R. Koerver, P. Braun, A. Weber, E. Ivers-Tiffée, T. Adermann, J. Kulisch, W. G. Zeier, F. H. Richter, J. Janek, *Nature Energy* **2020**, 5, 259; c)Y. Lu, Z. Tu, L. A. Archer, *Nat Mater* **2014**, 13, 961; d)Z. Hou, J. Zhang, W. Wang, Q. Chen, B. Li, C. Li, *Journal of Energy Chemistry* **2020**, 45, 7; e)S. Lou, F. Zhang, C. Fu, M. Chen, Y. Ma, G. Yin, J. Wang, *Adv Mater* **2021**, 33, e2000721; f)Z. Yu, X. Zhang, C. Fu, H. Wang, M. Chen, G. Yin, H. Huo, J. Wang, *Advanced Energy Materials* **2021**, 11; g)H. Wang, H. An, H. Shan, L. Zhao, J. Wang, *Acta Physico Chimica Sinica* **2020**, 0, 2007070.

[2] a)M. J. Lee, J. Han, K. Lee, Y. J. Lee, B. G. Kim, K. N. Jung, B. J. Kim, S. W. Lee, *Nature* **2022**, 601, 217; b)C. Yang, Q. Wu, W. Xie, X. Zhang, A. Brozena, J. Zheng, M. N. Garaga, B. H. Ko, Y. Mao, S. He, Y. Gao, P. Wang, M. Tyagi, F. Jiao, R. Briber, P. Albertus, C. Wang, S. Greenbaum, Y. Y. Hu, A. Isogai, M. Winter, K. Xu, Y. Qi, L. Hu, *Nature* **2021**, 598, 590; c)L. L.-l. PAN Xiao-na, WANG Zhi-pu, WANG Dan, LI Yun, YANG Pei-xia, ZHANG Jin-qiu, AN Mao-zhong, **2020**, 26, 406; d)G. Z.-l. LI Xue, **2020**, 26, 338; e)W.-Q. Wei, B.-Q. Liu, Y.-Q. Gan, H.-J. Ma, D.-W. Cui, *Rare Metals* **2020**, 40, 409; f)L. Dong, S. Zhong, B. Yuan, Y. Li, J. Liu, Y. Ji, D. Chen, Y. Liu, C. Yang, J. Han, W. He, *Angew Chem Int Ed Engl* **2023**, e202301073.

[3] a)X. Yang, K. Doyle-Davis, X. Gao, X. Sun, *eTransportation* **2022**, 11; b)X. Lu, S. R. Daemi, A. Bertei, M. D. R. Kok, K. B. O'Regan, L. Rasha, J. Park, G. Hinds, E. Kendrick, D. J. L. Brett, P. R. Shearing, *Joule* **2020**, 4, 2746; c)X. Judez, G. G. Eshetu, C. Li, L. M. Rodriguez-Martinez, H. Zhang, M. Armand, *Joule* **2018**, 2, 2208; d)R. Zhang, Y. Dong, M. A. Al-Tahan, Y. Zhang, R. Wei, Y. Ma, C. Yang, J. Zhang, *Journal of Energy Chemistry* **2021**, 60, 85; e)C.-L. Yan, *Rare Metals* **2020**, 39, 458.

[4] a)Z. Wang, X. Li, Y. Chen, K. Pei, Y.-W. Mai, S. Zhang, J. Li, *Chem* **2020**, 6, 2878; b)H. Yu, Y. Cao, L. Chen, Y. Hu, X. Duan, S. Dai, C. Li, H. Jiang, *Nat Commun* **2021**, 12, 4564; c)L. Wang, A. Dai, W. Xu, S. Lee, W. Cha, R. Harder, T. Liu, Y. Ren, G. Yin, P. Zuo, J. Wang, J. Lu, J. Wang, *J Am Chem Soc* **2020**, 142, 14966.

[5] Q. Zhao, P. Chen, S. Li, X. Liu, L. A. Archer, *Journal of Materials Chemistry A* **2019**, 7, 7823.

[6] a)S. Lou, Q. Liu, F. Zhang, Q. Liu, Z. Yu, T. Mu, Y. Zhao, J. Borovilas, Y. Chen, M. Ge, X. Xiao, W. K. Lee, G. Yin, Y. Yang, X. Sun, J. Wang, *Nat Commun* **2020**, 11, 5700; b)Y.-J. S. Xue Sun, Ren-Long Li, Jia-Jun Wang, **2022**, 28, 2214011; c)X. S. Ya-Jie Song, Li-Ping Ren, Lei Zhao, Fan-Peng Kong, Jia-Jun Wang, **2022**, 28, 2108461.

[7] a)X. Wang, Y. Song, X. Jiang, Q. Liu, J. Dong, J. Wang, X. Zhou, B. Li, G. Yin, Z. Jiang,

J. Wang, *Advanced Functional Materials* **2022**, 32; b)J. Qiu, X. Liu, R. Chen, Q. Li, Y. Wang, P. Chen, L. Gan, S. J. Lee, D. Nordlund, Y. Liu, X. Yu, X. Bai, H. Li, L. Chen, *Advanced Functional Materials* **2020**, 30; c)M. Nakayama, S. Wada, S. Kuroki, M. Nogami, *Energy & Environmental Science* **2010**, 3.

[8] M. M. Besli, S. Xia, S. Kuppan, Y. Huang, M. Metzger, A. K. Shukla, G. Schneider, S. Hellstrom, J. Christensen, M. M. Doeff, Y. Liu, *Chemistry of Materials* **2018**, 31, 491.

[9] X. Lu, A. Bertei, D. P. Finegan, C. Tan, S. R. Daemi, J. S. Weaving, K. B. O'Regan, T. M. M. Heenan, G. Hinds, E. Kendrick, D. J. L. Brett, P. R. Shearing, *Nat Commun* **2020**, 11, 2079.

[10]R. J. Chen, Y. B. Zhang, T. Liu, B. Q. Xu, Y. H. Lin, C. W. Nan, Y. Shen, *ACS Appl Mater Interfaces* **2017**, 9, 9654.

[11]J. Wang, L. Wang, C. Eng, J. Wang, *Advanced Energy Materials* **2017**, 7.

[12]C. Fu, S. Lou, X. Xu, C. Cui, C. Li, P. Zuo, Y. Ma, G. Yin, Y. Gao, *Chemical Engineering Journal* **2020**, 392.

[13]B. Zahiri, A. Patra, C. Kiggins, A. X. B. Yong, E. Ertekin, J. B. Cook, P. V. Braun, *Nat Mater* **2021**, 20, 1392.

[14]H. Cha, J. Kim, H. Lee, N. Kim, J. Hwang, J. Sung, M. Yoon, K. Kim, J. Cho, *Adv Mater* **2020**, 32, e2003040.

[15]B. Li, K. Kumar, I. Roy, A. V. Morozov, O. V. Emelyanova, L. Zhang, T. Koc, S. Belin, J. Cabana, R. Dedryvere, A. M. Abakumov, J. M. Tarascon, *Nat Mater* **2022**, 21, 1165.

[16]N. Sun, Y. Song, Q. Liu, W. Zhao, F. Zhang, L. Ren, M. Chen, Z. Zhou, Z. Xu, S. Lou, F. Kong, J. Wang, Y. Tong, J. Wang, *Advanced Energy Materials* **2022**, 12.

[17]N. Wu, P. H. Chien, Y. Qian, Y. Li, H. Xu, N. S. Grundish, B. Xu, H. Jin, Y. Y. Hu, G. Yu, J. B. Goodenough, *Angew Chem Int Ed Engl* **2020**, 59, 4131.

[18]a)S. Tan, Z. Shadike, J. Li, X. Wang, Y. Yang, R. Lin, A. Cresce, J. Hu, A. Hunt, I. Waluyo, L. Ma, F. Monaco, P. Cloetens, J. Xiao, Y. Liu, X.-Q. Yang, K. Xu, E. Hu, *Nature Energy* **2022**, 7, 484; b)T. Liu, L. Yu, J. Liu, J. Lu, X. Bi, A. Dai, M. Li, M. Li, Z. Hu, L. Ma, D. Luo, J. Zheng, T. Wu, Y. Ren, J. Wen, F. Pan, K. Amine, *Nature Energy* **2021**, 6, 277.

[19]Y. Xiao, K. Turcheniuk, A. Narla, A. Y. Song, X. Ren, A. Magasinski, A. Jain, S. Huang, H. Lee, G. Yushin, *Nat Mater* **2021**, 20, 984.

[20]J. Ma, Z. Liu, B. Chen, L. Wang, L. Yue, H. Liu, J. Zhang, Z. Liu, G. Cui, *Journal of The Electrochemical Society* **2017**, 164, A3454.

[21]a)Q. S. Liu, H. W. An, X. F. Wang, F. P. Kong, Y. C. Sun, Y. X. Gong, S. F. Lou, Y. F. Shi, N. Sun, B. Deng, J. Wang, J. J. Wang, *Natl Sci Rev* **2023**, 10, nwac272; b)Z. Xiong, Z. Wang, W. Zhou, Q. Liu, J.-F. Wu, T.-H. Liu, C. Xu, J. Liu, *Energy Storage Materials* **2023**, 57, 171.

Simultaneously achieving high-energy cathode and long cycle life is still challenged by the interfacial stability under high-voltage and high loadings. Here we revealed the role of cathode structure on electrochemical stability of electrolytes. This diagnosis inspired a universal and practical electrode fabrication method, enabling all-solid-state batteries with high loading to exhibit extremely long cyclic time at high cut-off voltages.

H. W. An, Q. S. Liu, B. Deng, J. Wang, M. L. Li, X. Li*, S. F. Lou*, J. J. Wang*

Negating Electrolyte Failure in Cathode for Long-Lifespan Solid-State Batteries
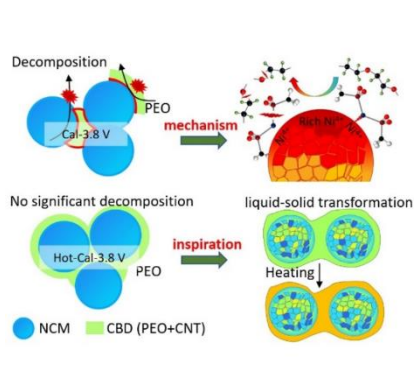
Supporting Information

Eliminating Local Electrolyte Failure induced by Asynchronous Reaction for High-Loading and Long-Lifespan All-Solid-State Batteries

H. W. An, Q. S. Liu, B. Deng, J. Wang, M. L. Li, X. Li*, S. F. Lou*, J. J. Wang*

Experimental Methods

Preparation of solid-state electrolyte:. The solid polymer electrolytes were prepared by a solution casting method and hot pressing. 2.763 g Polyethylene oxide (PEO, Mn = 600,000, Aladdin, 98%) and 1 g lithium bis(trifluoromethane sulfonimide) (LiTFSI, Aladdin, 97%) were added into 60 ml anhydrous acetonitrile (ACN, Aladdin, 99%) solutions, the EO:Li ratio is 18:1. After stirring for 12 hours, 0.663 g $Li_{6.4}La_3Zr_{1.4}Ta_{0.6}O_{12}$ (LLZTO) were added to the above homogeneous solution, after stirring for another 12 hours, the mixture was poured into a polytetrafluoroethylene mold and dried under vacuum at 60 °C for 48 h. Finally, a solid-state electrolyte (PEO-LiTFSI-LLZTO) membrane was obtained through hot pressing process. The preparation of PEO-LiTFSI electrolyte is similar to the above method except for the addition of LLZTO step.

Preparation of solid-state composite cathode: Firstly, $LiNi_{0.8}Co_{0.1}Mn_{0.1}O_2$, PEO-LiTFSI, and carbon nanotubes (CNTs) were added to N-Methyl pyrrolidone (NMP, Aladdin, 98%) solvent in a mass ratio of 80:15:5 to form electrode slurry, in which PEO-LiTFSI was prepared in advance as an electrolyte solution with a content of 5% in acetonitrile as the solvent. After stirring for 24 hours, then the obtained uniform slurry was coated on the aluminum current collector, with a coating blade height of 0.45 mm. Subsequently, the electrode is dried at 65 °C for 24 h under vacuum to eliminate residual solvent. Finally, the dried cathodes were pressed at a pressure of 1 MPa cm^{-2}, then the calendaring cathodes were obtained. To prepare the Hot-calendaring cathodes, press the dried cathode to 1 MPa cm^{-2} at 80 °C.

Preparation of fully active surface cathode: In a glovebox filled with argon ($H_2O < 0.01$ ppm and $O_2 < 0.01$ ppm), 2.625 g poly(ethylene glycol)diacrylate (PEGDA, Mn =1000, Aladdin, 98%), 0.138 g ethyl cyanoacrylate (ECA, Macklin, 99%), 0.028 g azodiisobutyronitrile (AIBN) and 1 g LiTFSI were mixed into an opaque glass bottle to stir 2 h, the precursor solution was

obtained. Then the $LiNi_{0.8}Co_{0.1}Mn_{0.1}O_2$, precursor solution and CNTs were well mixed in a mortar, the corresponding mass ratio is 80:15:5 (**Figure S12**). Finally, the obtained mixture was uniformly applied onto aluminum foil for in-situ polymerization at 80 °C for 8 h, and a non-porous electrode was finally prepared.

Electrochemical measurements: The CR2025 coin-type full batteries were assembled at a sealing pressure of 0.65 T in glovebox filled with argon, where the lithium metal foil is used as the anode, the PEO-LiTFSI-LLZTO is used as solid-state electrolyte membrane, and different composite cathodes as working cathodes, all the cathode with loading over 12 mg cm^{-2}. Galvanostatic intermittent titration technique (GITT) and galvanostatic charge/discharge measurements were performed on Neware battery test system (BTS-2004, Shenzhen, China) under 60 °C, and the voltage ranges of Li|SPE|NCM811 were adjusted to 2.8-4.2 V. For the GITT procedure, the current density is 0.1 C, the charging process time is is set 30 min, and the relaxation time is set to 30 min. The lithium-ion diffusion coefficient (D)was calculated by equation (1):

$$D = \frac{4}{\pi t} \left(\frac{R_s}{3} \right)^2 \left(\frac{\Delta E_s}{\Delta E_\tau} \right)^2 \tag{1}$$

where R_s represents the average radius of active material particles. The active material used in all composite cathodes in this study is the same, so the formula can be normalized to the following equation (2):

$$D_1 = \frac{D}{\frac{4}{\pi t} \left(\frac{R_s}{3} \right)^2} = \left(\frac{\Delta E_s}{\Delta E_\tau} \right)^2 \tag{2}$$

Therefore, D_1 can be used to represent the normalized lithium-ion diffusion coefficient in each cathode, and ΔE_s and ΔE_τ are the change of the steady-state voltage and the total change of cell voltage during a constant pulse of a single-step GITT experiment.

The ionic conductivity of electrolyte films and all electrochemical impedance polymer electrolytes was evaluated by the electrochemical working station (Par-Solartron 663). The SS|PEO-LiTFSI|SS batteries were assembled with stainless steel sheet and electrolyte membrane. Ionic conductivity is calculated by the equation (3):

$$\sigma = \frac{L}{RS} \tag{3}$$

where L represents thickness the of electrolyte membrane, the R resistance of battery and S the contact area between steel sheet and electrolyte. The electrochemical window of the SPE was

conducted by linear sweep voltammetry (LSV) technique in a battery that sandwiched the electrolyte between steel sheet and lithium metal at a sweep rate of 1 mV s^{-1}, 60 °C.

SEM, XRD, FTIR, and Raman: The morphology of cathode and powders were observed by field-emission scanning electron microscopy (SEM, Phenom Pro), and the smooth cross-section of the cathode was achieved by a cross-section ion polisher (accelerating voltage: 2~6 kV, beam spot size: 500 μm). Powder X-ray diffraction (XRD) patterns of active materials were recorded using X-ray powder diffractometer (Philips, Holland, Cu Kα radiation (λ = 1.5418 Å).) Fourier transforms infrared (FTIR) spectra were recorded by FTIR-8400S Spectrophotometer of Shimadzu. The in-situ experiment was performed by punching holes in the battery case, lithium metal foil, and aluminum foil, and sealing the holes of the battery case with a transparent CaF_2 substrate. Raman spectrum was recorded by Raman spectrometer (Renishaw), the active particles were located by high-resolution optical microscopy. All batteries were disassembled in the glovebox filled with argon. The mutual reaction energy of electrolyte and the active materials was calculated using material energies obtained from the Materials Project (MP) database.

Transmission X-ray microscopy (TXM) and corresponding data analysis: The CT image of TXM with synchrotron X-ray was recorded at Shanghai Synchrotron Radiation Facility (SSRF), beamline BL13W1. At above 20keV, for ~900 projections over an angular range of 180° with a field of view of 1×1 mm^2 (with a 2k×2k CCD camera binning 2×2 camera pixels into one output pixel). The raw data obtained is tomographically aligned and reconstructed. The reconstructed cathode 3D data was further processed by the software package Avizo (Thermo Fisher Scientific, Waltham, Massachusetts, USA) for 3D visualization and quantized data analysis.

Scanning transmission X-ray microscopy (STXM) and STXM-Ptychography: The two samples were disassembled from the calendaring electrode and the hot- calendaring electrode, respectively, and the particles were obtained by methanol/ethanol sonication. The STXM experiments were performed at the beamline 10ID-1 SM, CLS. The STXM data were recorded in the same environment, with a scanned image size of 2.5×2.5 μm^2 (80×80 points). The open-source software aXis2000 (McMaster University, Canada) was used to perform principal component analysis-cluster analysis (PCA-CA) of the active materials on the STXM energy stack data sets with the angular distance measurement mode (cutoff value 0.01).

For the STXM-ptychography experiments, a 35 nm outer-zone-width zone plate was used to focus the monochromatic soft X-ray beam, and the sample was placed off the focal point to have a beam spot with a size of 2 μm on the sample. A sample raster scan (16×16 pixels) in 0.5 μm increments were used to ensure sufficient overlap of the scanned area. An order-sorting aperture with a size of 50 μm was used to block all but the first-order beam from the zone plate. Diffraction data were recorded on a CCD camera (2048×2052 pixels), which was cooled to −40 °C and placed 59.5 mm downstream of the sample. The sample position is stabilized with respect to the zone plate by an interferometer that measures relative displacements in the scanning directions with 10 nm resolution. To analyze the active materials using STXM-ptychography at multiple elemental edges in a single ptychography stack scan, spectro-ptychography, the photon energies were chosen to be Ni L-edge (845, 852.0, and 854.4 eV), with an energy resolution of $\Delta E/E = 1 \times 10^{-4}$.
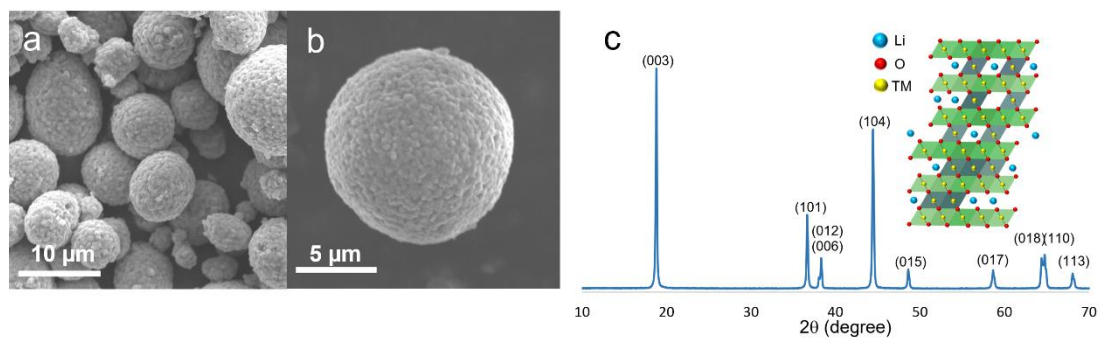
Figure S1. (a) Scanning Electron Microscope image of Commercial $LiNi_{0.8}Co_{0.1}Mn_{0.1}O_2$ polycrystalline particles with scale bar 10 µm and (b) 5 µm. (c) X-ray diffraction patterns of $LiNi_{0.8}Co_{0.1}Mn_{0.1}O_2$ particles.
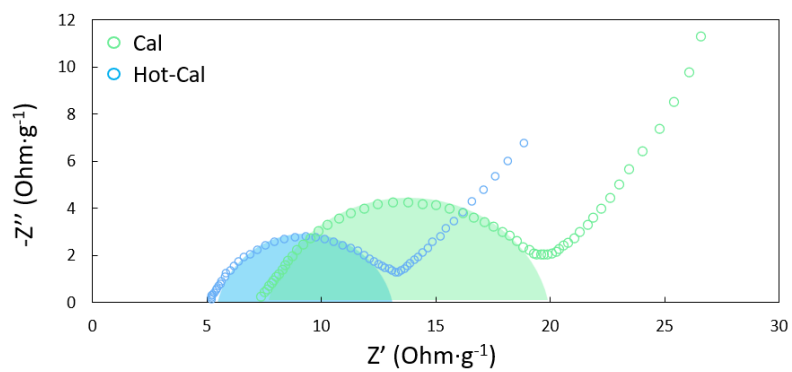
Figure S2. Electrochemical Impedance Spectroscopy of calendaring cathode and Hot-calendaring cathode.
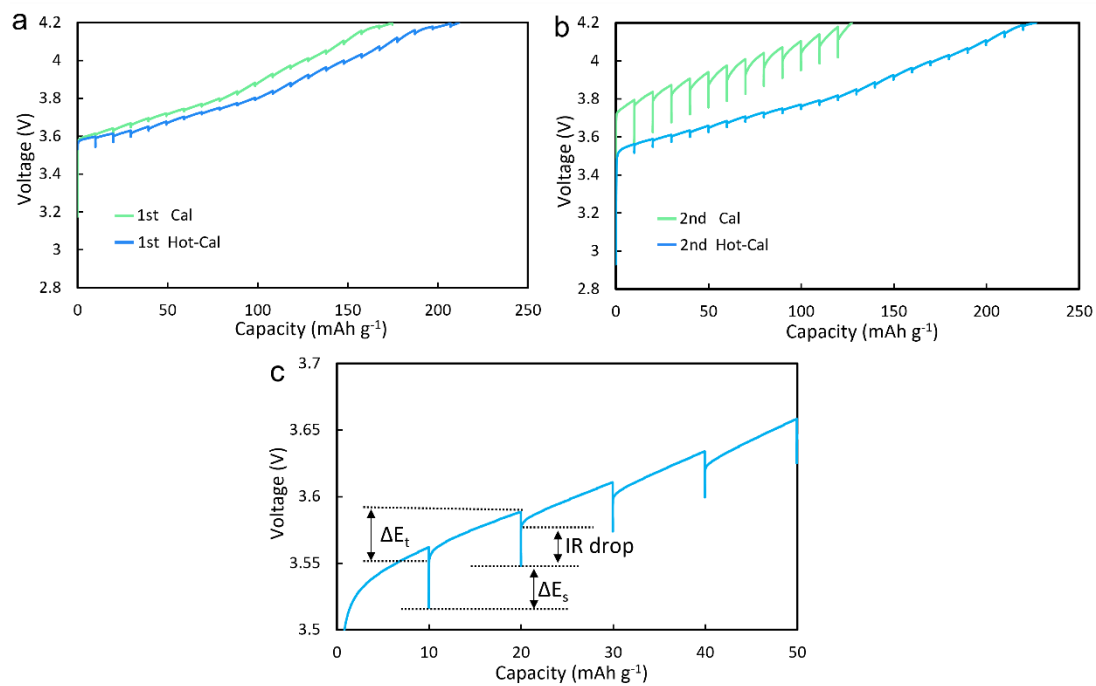
Figure S3. (a) Galvanostatic intermittent titration technique (GITT) curve of calendaring cathode and Hot-calendaring cathode at first cycle and (b) second cycle. (c) Enlarged GITT curve.
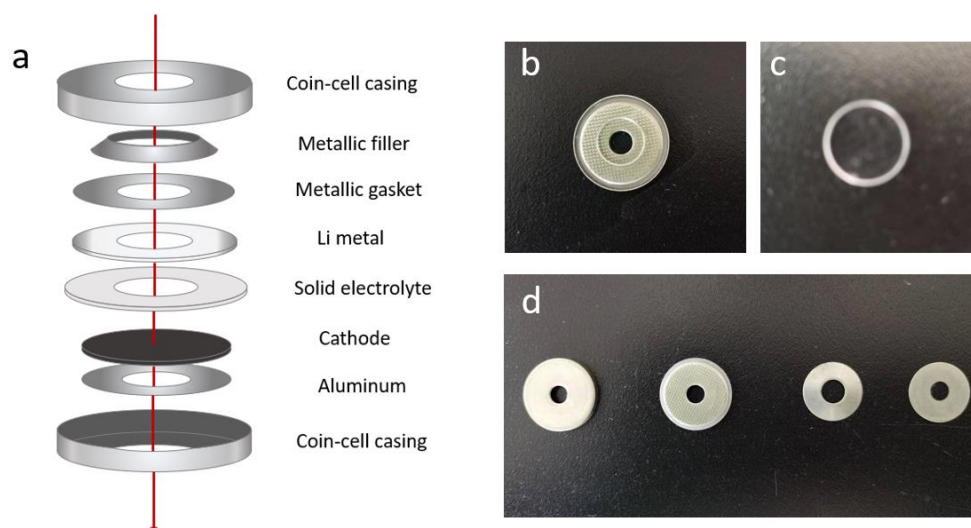
Figure S4. (a) The schematic diagram of in-situ FTIR cell structure. (b) The photo of in-situ FTIR cell and the (c) $CaCl_2$ substrate; (d) The photo of coin-cell casing, metallic filler and metallic gasket.

25
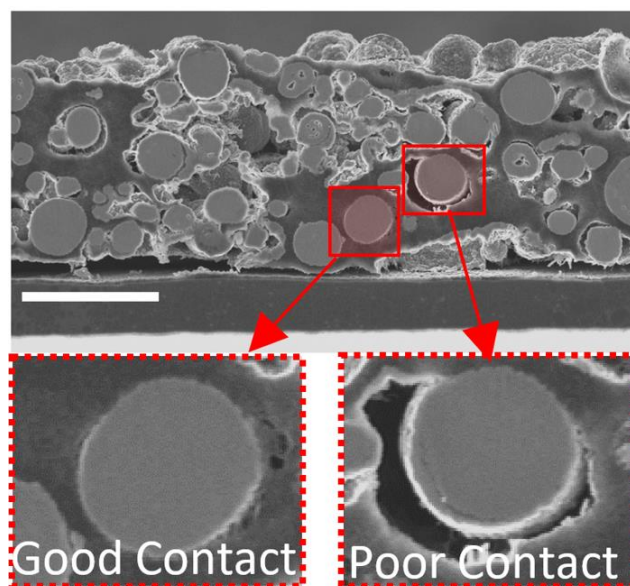
Figure S5. Scanning Electron Microscope image of good and poor contact particle in cathode.

WILEY-VCH
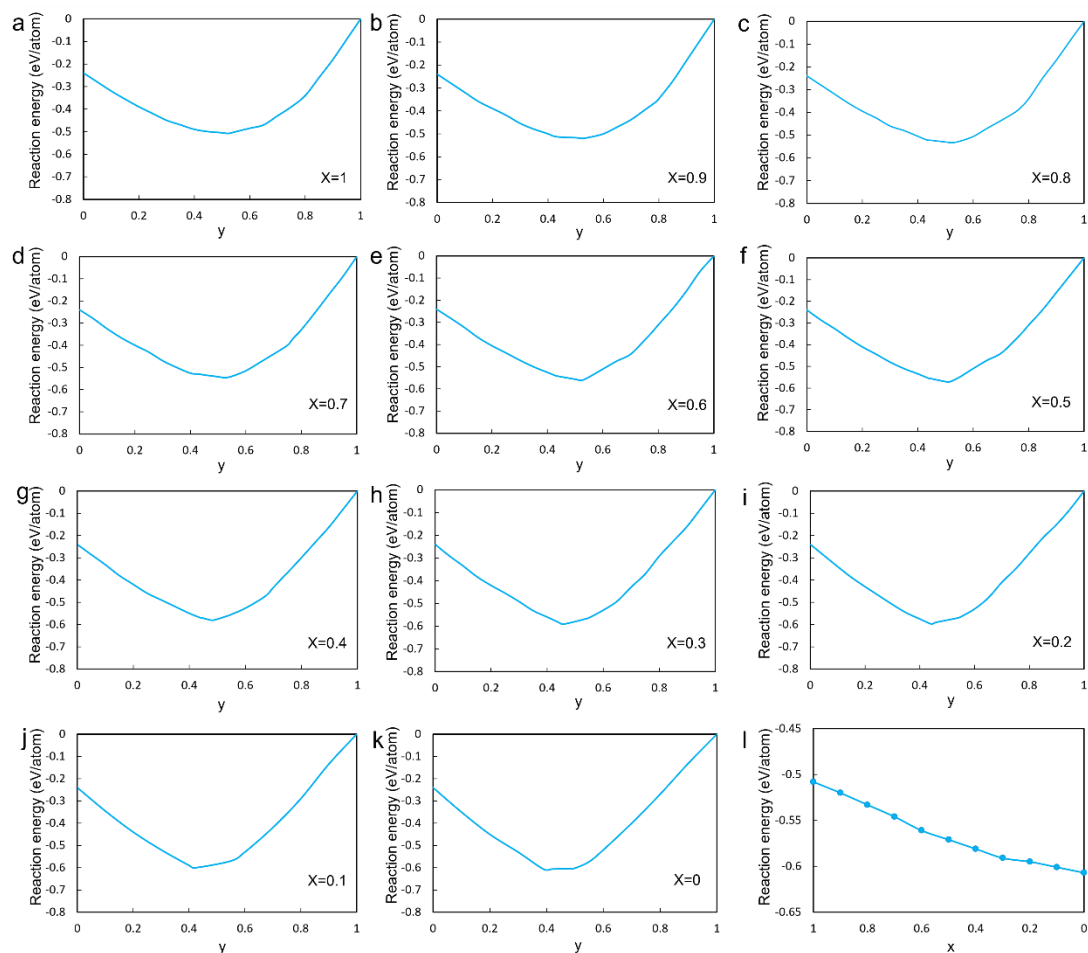
Figure S6. (a) Interface reaction energy between $Li_xNi_{0.8}Co_{0.1}Mn_{0.1}O_2$ and LiTFSI, in which x is 1 and (b-k) x is from 0.9 to 0, y is the molar fraction of $Li_xNi_{0.8}Co_{0.1}Mn_{0.1}O_2$ in the reaction [y $Li_xNi_{0.8}Co_{0.1}Mn_{0.1}O_2$+(1-y) LiTFSI]. (l) Variation of reaction energy with the degree of delithiation (Curve of reaction energy versus x).

27
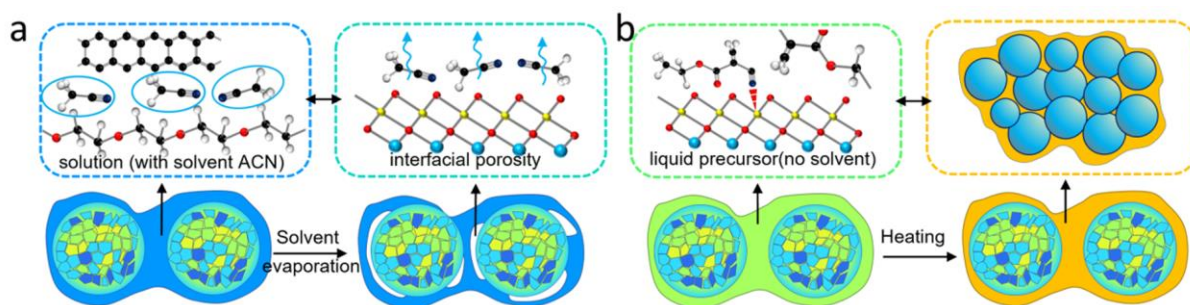
**Figure S7.** (a) Fabrication process of the traditional organic solid-state cathode. (b) Rational design and modification mechanism of cathode.
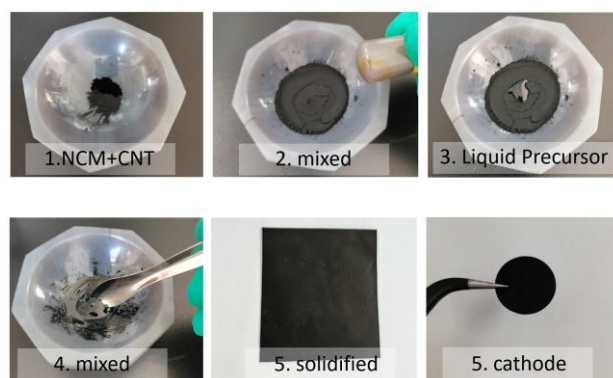
Figure S8. Preparation process of fully active surface electrode.
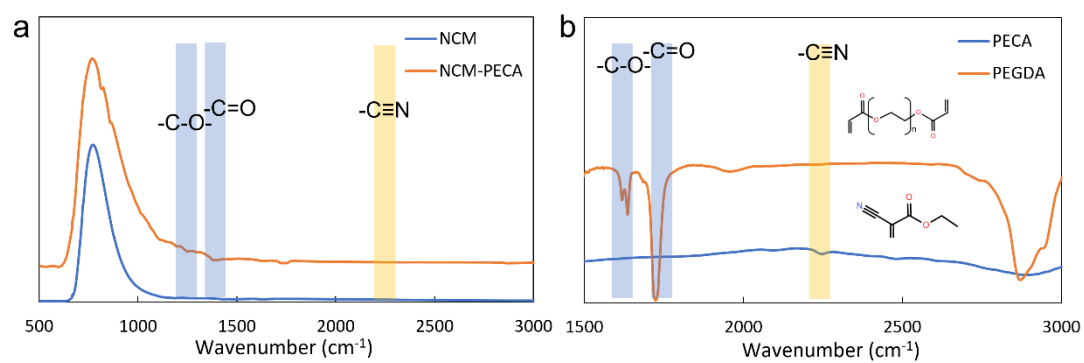
Figure S9. (a) Fourier transform infrared spectroscopy (FTIR) of $LiNi_{0.8}Co_{0.1}Mn_{0.1}O_2$ and $LiNi_{0.8}Co_{0.1}Mn_{0.1}O_2$-[poly(ethylene glycol)diacrylate-poly(ethyl cyanoacrylate)]. (b) FTIR of poly(ethylene glycol)diacrylate and poly(ethyl cyanoacrylate).
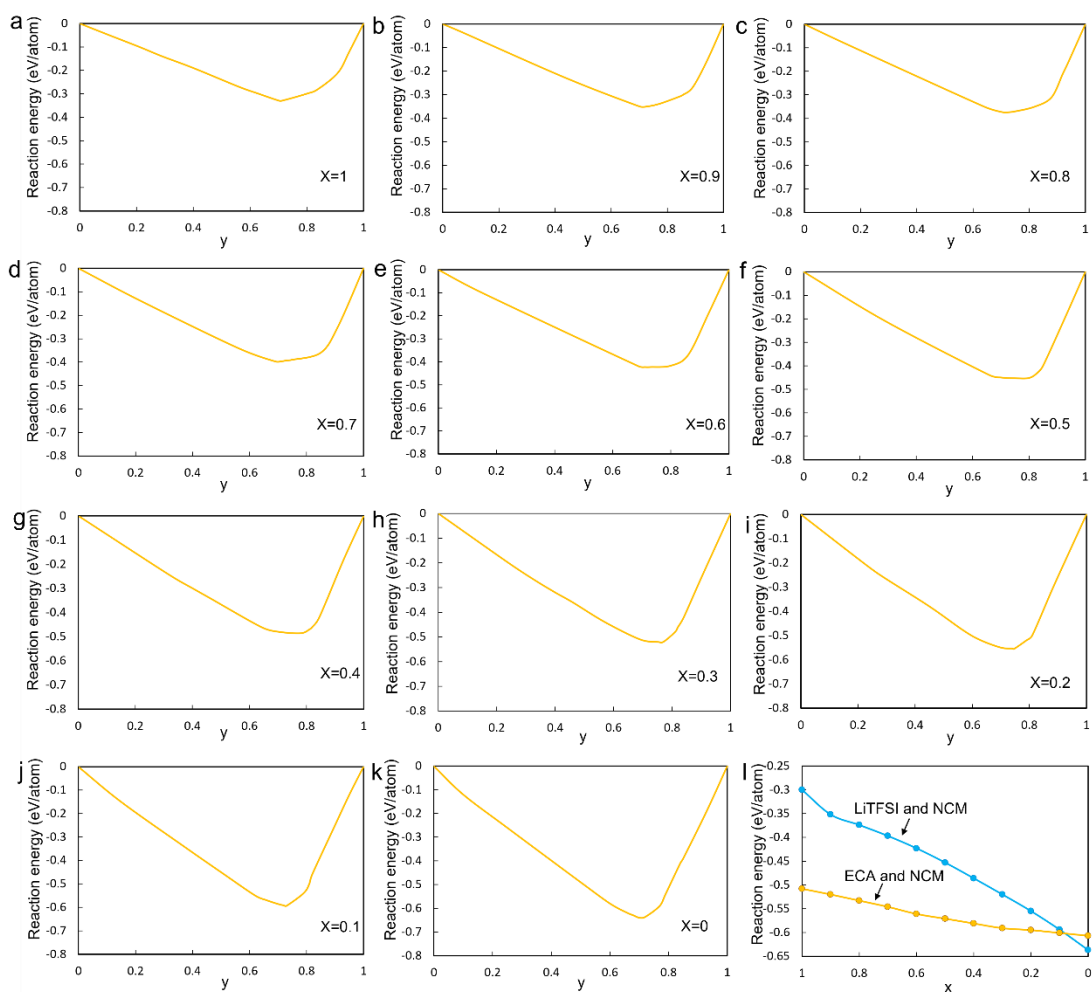
Figure S10. (a) Interface reaction energy between $Li_xNi_{0.8}Co_{0.1}Mn_{0.1}O_2$ and ethyl cyanoacrylate (ECA), in which x is 1 and (b-k) x is from 0.9 to 0, y is the molar fraction of $Li_xNi_{0.8}Co_{0.1}Mn_{0.1}O_2$ in the reaction [y $Li_xNi_{0.8}Co_{0.1}Mn_{0.1}O_2$+(1-y) ECA]. (l) Variation of reaction energy with the degree of delithiation (Curve of reaction energy versus x).
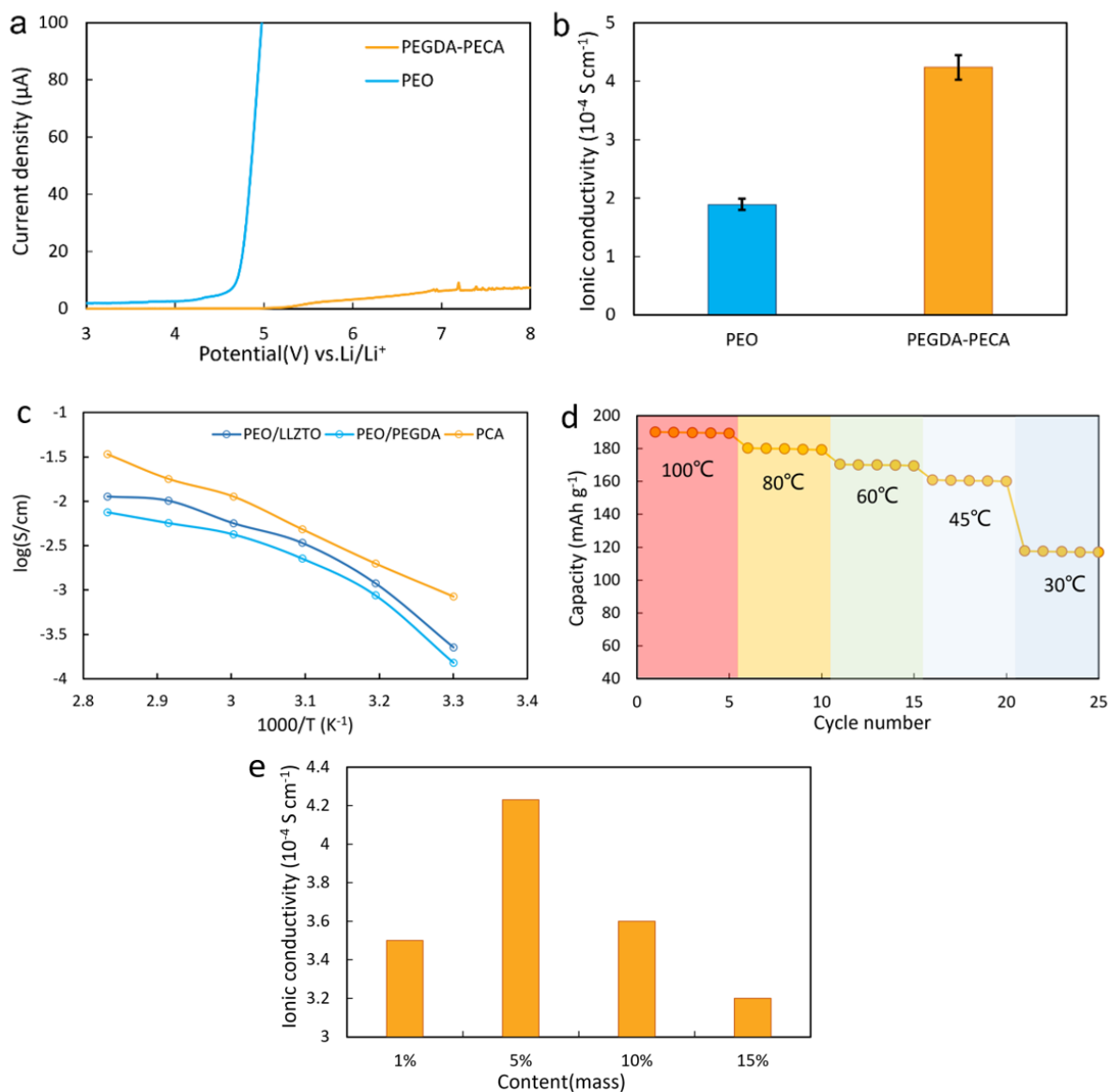
Figure S11. (a) Linear sweep voltammetry comparison of poly(ethylene glycol)diacrylate-poly(ethyl cyanoacrylate) (PEGDA-PECA) electrolyte and polyethylene oxide (PEO) electrolyte. (b) Ionic conductivity of PEGDA-PECA electrolyte and PEO electrolyte. (c) Conductivity and temperature curves of different electrolytes. (d) Discharge capacity of PCA battery at different temperatures. (e) Ionic conductivity of PEGDA-PECA electrolyte with different ECA content.

WILEY-VCH
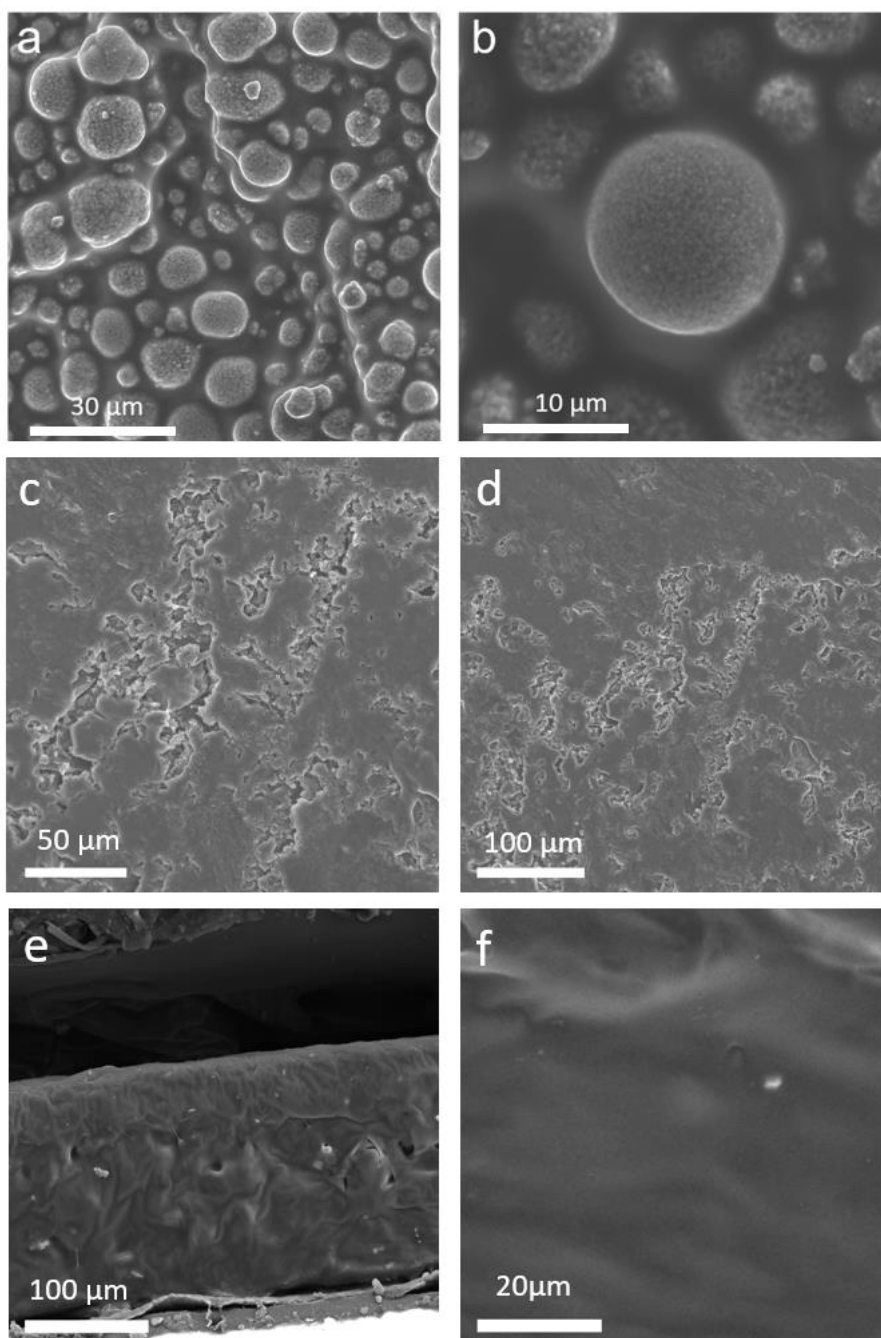
Figure S12. (a) Scanning Electron Microscope(SEM) image of surface of the non-pore cathode with scale bar 30 µm and (b) 10 µm. (c) SEM of Li metal surface from recycled PCA battery with scale bar 50 µm and (d) 100 µm. (e) Cross section and (d) surface of PEO-LLZTO.
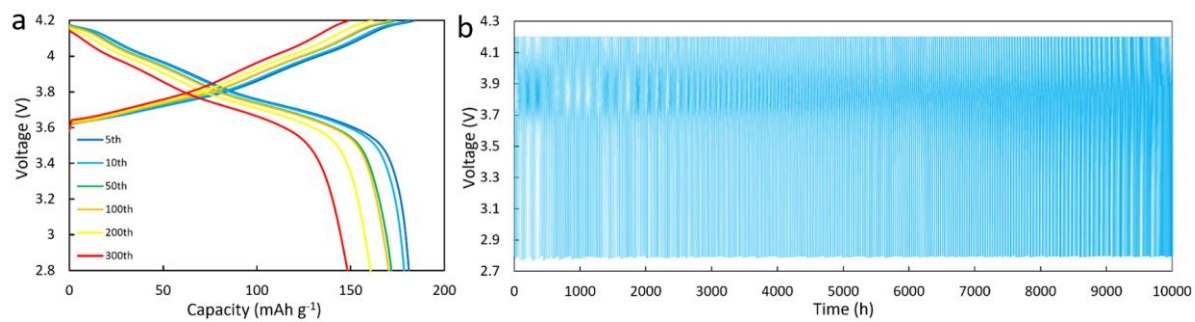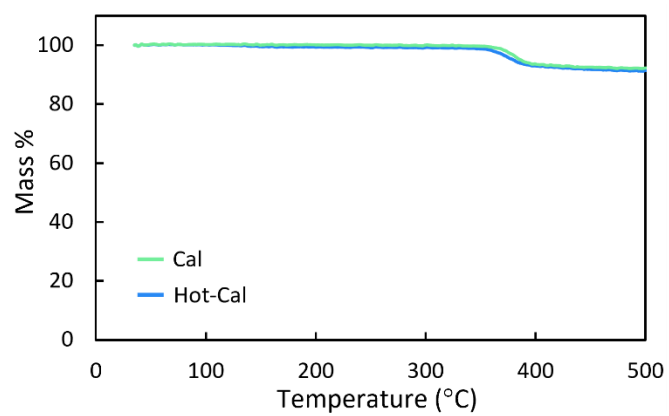
**Figure S13.** (a)Charging/discharging profiles of non-pore cathode. (b) Time-voltage curve of PCA.
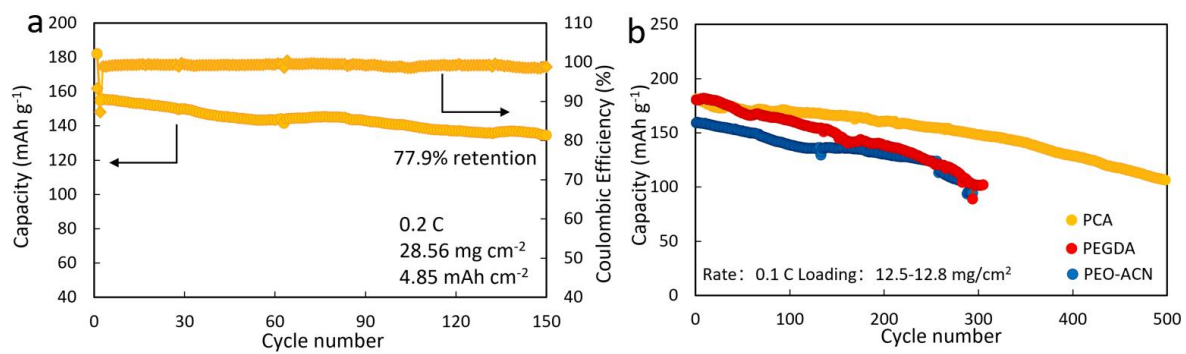
Figure S14. (a) Cyclic performance of PCA batteries with loading of 28.6mg cm^{-2}. (b) Battery cycle performance comparison of PCA, PEGDA and PEO-ACN cathode.
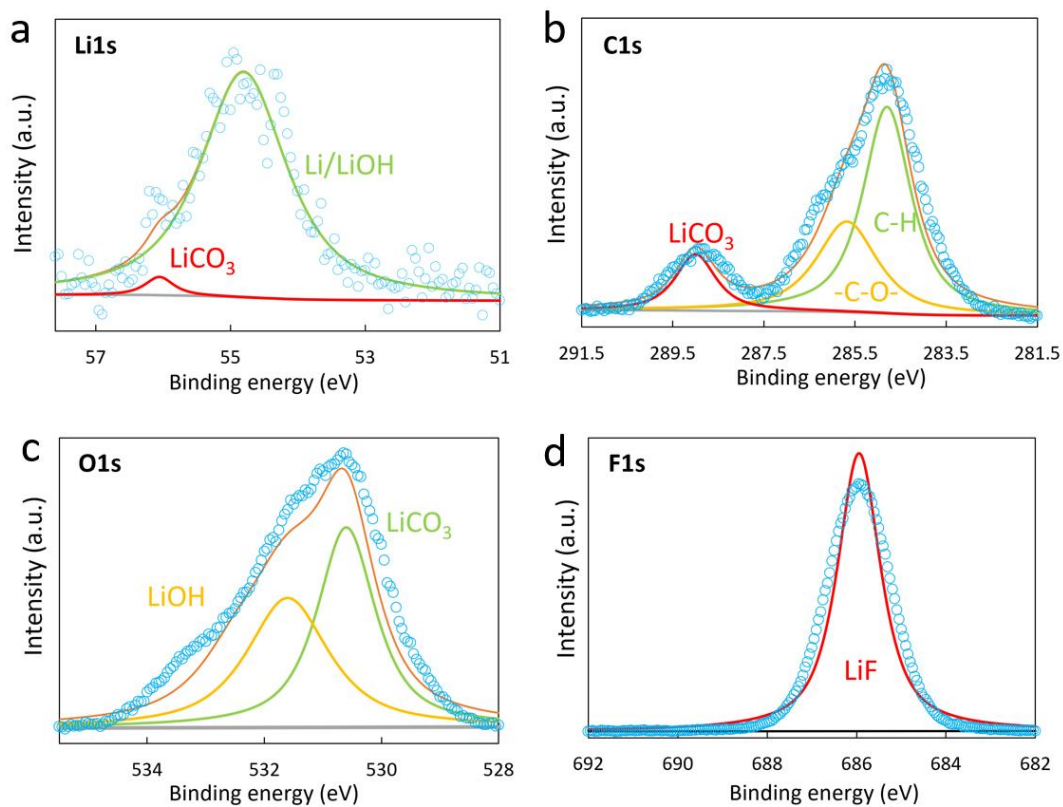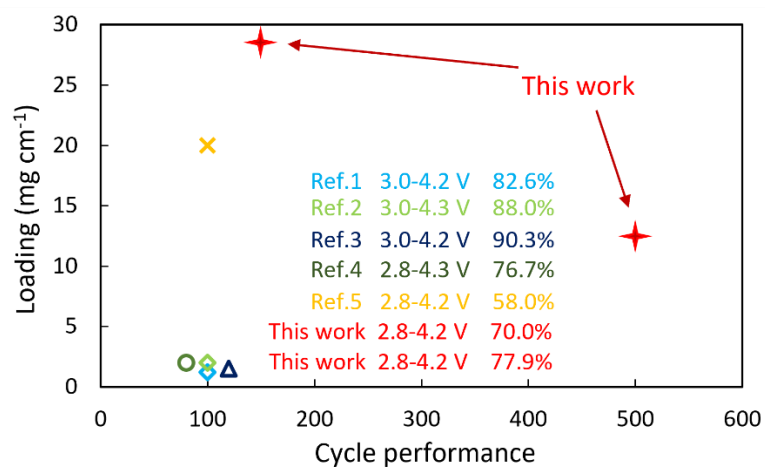
Figure S15. X-ray photoelectron spectroscopy of Li metal surface from recycled PCA battery, (a) Li1s; (b) C1s; (c) O1s; (d) F1s.

Figure S16. Thermos-Gravimetric curves of Cal and Hot-Cal cathodes.
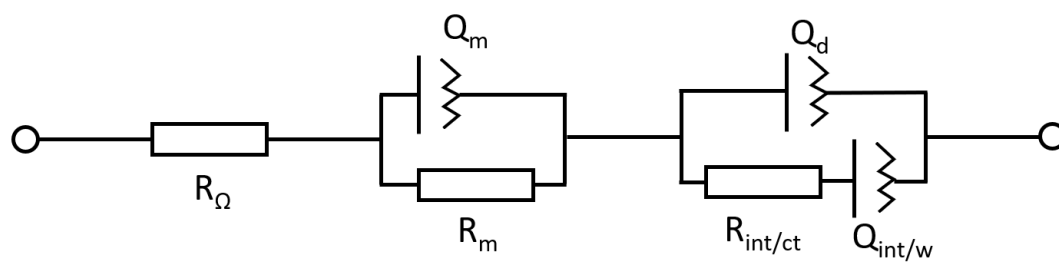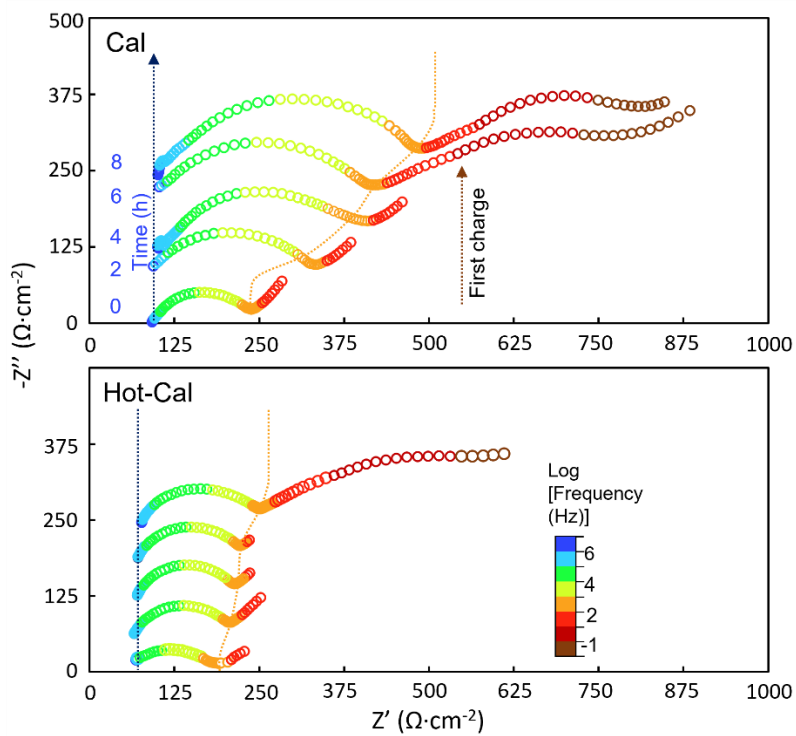
Figure S17. Equivalent circuit diagram of the battery.

Figure S18. Statistics of loading and cycle performance for reported PEO-based high-voltage solid-state battery.

Figure S19. Comparison of interface impedance evolution during first charging, as well as the image of poor contact and good contact particle (Ω cm^{-2}).